

THE GLOBULAR CLUSTER SYSTEM IN M87: A WIDE-FIELD STUDY WITH CFHT/MEGACAM*

WILLIAM E. HARRIS

Department of Physics & Astronomy, McMaster University, Hamilton ON L8S 4M1

Draft version July 6, 2018

ABSTRACT

CFHT Megacam data in (g', r', i') are used to obtain deep, wide-field photometry of the globular cluster system (GCS) around M87. A total of 6200 GCs brighter than $i' = 23.0$ (roughly equivalent to $M_I = -8.5$) are included in the study, essentially containing almost the entire bright half of the total GC population in the galaxy. The classic bimodal metal-poor and metal-rich sequences of GCs show up clearly; while the spatial distribution of the GCs can be traced detectably outward to $R_{gc} \simeq 100$ kpc and perhaps further, the blue, metal-poor subpopulation is very much more spatially extended than the red subpopulation. Both the red and blue GC subsystems have radial metallicity gradients, where mean heavy-element abundance scales with projected galactocentric distance as $Z \sim R^{-0.12}$ (blue) and $R^{-0.17}$ (red). The blue sequence exhibits a strongly significant mass/metallicity relation (MMR) in which the mean metallicity gradually increases with cluster luminosity as $Z \sim L^{0.25 \pm 0.05}$ for the luminosity range $M_I \lesssim -10$ and the assumption of a constant M/L . However, this relation is also clearly nonlinear: fainter than this level, the sequence is more nearly vertical. This mass/metallicity trend can be understood as the result of self-enrichment within the most massive metal-poor GCs during their formation. The red sequence formally exhibits a negatively sloped MMR, but the numerical solutions and tests show that this red-GC slope is not very significant. In giant elliptical galaxies, the red GCs are likely to represent a broad composite population formed during several major starbursts. If so, the red sequence might display a *population-based* MMR that could in principle be either positive or negative.

Subject headings: galaxies: elliptical and lenticular, cD

1. INTRODUCTION

By far the largest collection of globular clusters (GCs) within any one galaxy in the local universe is in M87, the cD giant in the Virgo cluster. Its total GC population is $N \simeq 14000$ (McLaughlin et al. 1994; Tamura et al. 2006), roughly a third of the GCS population in all the Virgo galaxies combined (see the Virgo Cluster Survey results of Peng et al. 2006). In addition, because both the foreground reddening and field contamination are low, the M87 GCS can be traced outward to extremely large projected galactocentric distance, 100 kpc or more (Tamura et al. 2006). This combination of characteristics makes M87 a unique testbed for systematics of GC systems.

A particular topic of recent interest is the correlation between GC metallicity and luminosity (or mass), a trend which has been found to show up on the blue, metal-poor sequence (Harris et al. 2006; Strader et al. 2006; Mieske et al. 2006; Spitler et al. 2006; Forte et al. 2007; Wehner et al. 2008; Bassino et al. 2008; Harris 2009, and references cited there). In brief, the mean GC metallicity along the blue sequence is seen to increase steadily,

though perhaps not linearly, with increasing cluster mass. So far, the most likely physical explanation that has been advanced for the origin of this effect is some form of self-enrichment during the protocluster epoch (Harris et al. 2006; Mieske et al. 2006; Strader & Smith 2008; Bailin & Harris 2009). The essential idea of this interpretation is that any self-enrichment should be more efficient within the more massive, deeper potential wells of the larger clusters.

M87 has turned into something of a flashpoint for discussion of this mass/metallicity relation (MMR). Strader et al. (2006) first claimed that the mean GC color along the entire blue sequence increased roughly linearly with absolute magnitude, which would correspond to a simple power-law scaling of heavy-element abundance with cluster mass, $Z \sim M^p$, for a constant mass-to-light ratio. Their measurements consisted of simple fixed-aperture photometry of ~ 1000 GCs around M87 from the single-orbit exposures in (g', z') of the galaxy that were taken as part of the Virgo Cluster Survey (Côté et al. 2004). Mieske et al. (2006) used the same material in the full Virgo Cluster Survey analysis in which the cluster photometry was done with PSF-convolved King profiles. They found much the same trend though it was less clear that the MMR was as straightforward as a linear fit in the color-magnitude plane. Forte et al. (2007) used ground-based C, T_1 photometry with standard PSF-fitting photometry, and found a roughly linear correlation of $(C - T_1)$ color versus magnitude along the blue sequence. Waters et al. (2009), on other hand, find no net MMR along the blue sequence (that is, they find a vertical sequence of magni-

*THIS RESEARCH USED THE FACILITIES OF THE CANADIAN ASTRONOMY DATA CENTRE OPERATED BY THE NATIONAL RESEARCH COUNCIL OF CANADA WITH THE SUPPORT OF THE CANADIAN SPACE AGENCY. BASED ON OBSERVATIONS OBTAINED AT THE CANADA-FRANCE-HAWAII TELESCOPE (CFHT) WHICH IS OPERATED BY THE NATIONAL RESEARCH COUNCIL OF CANADA, THE INSTITUT NATIONAL DES SCIENCES DE L'UNIVERS OF THE CENTRE NATIONAL DE LA RECHERCHE SCIENTIFIQUE OF FRANCE, AND THE UNIVERSITY OF HAWAII. Electronic address: harris@physics.mcmaster.ca

tude versus color) by using size-corrected aperture photometry of about 2000 clusters from deeper HST/ACS images of M87 in (V, I) . Most recently, Peng et al. (2009) have analyzed the same ultra-deep HST/ACS data with the PSF-convolved King profile technique described in Jordán et al. (2009) to find that a significant color/magnitude slope exists for the upper half of the GC magnitude range (roughly, for the clusters brighter than the turnover point of their luminosity function). Thus five different measurement procedures from four partially different datasets have yielded results that are largely in mutual agreement, but also show points of disagreement that are still of some importance and need to be settled.

For comparison, the largest GC database used specifically to analyze the MMR is the sample of $\sim 10,000$ clusters in six giant Brightest Cluster Galaxies (Harris 2009). There, the photometry of the individual GCs is obtained from PSF-convolved King-model profiles and is taken in the metallicity-sensitive $(B - I)$ index and with deep exposures.¹ For clusters brighter than the GCLF turnover the data have high S/N, and the total sample is so large that the GCLF can be traced upward to the most luminous known GCs at $L \gtrsim 10^7 L_\odot$. Extensive evidence is presented that the MMR has a nonlinear form: the blue GC sequence is nearly vertical (i.e., no trend of GC color versus luminosity) for $L \lesssim 5 \times 10^5 L_\odot$ and then curves toward redder color at higher luminosity.

The quantitative self-enrichment model of Bailin & Harris (2009) reproduces this nonlinear MMR form fairly accurately. The key physical point in the model is that protoclusters less massive than about $10^6 M_\odot$ do not have deep enough potential wells to hold back much of the first round of SNII-enriched gas, so for these lower-mass GCs there should be no MMR on *either* the blue or red sequence. Conversely, for the higher-mass GCs with their deep potential wells, self-enrichment is almost automatically required. A unique prediction of this particular model is that *both* the red and blue GC sequences should exhibit a MMR at the top end, though it should be less noticeable for the red sequence because it starts from a much higher level of pre-enrichment.

Settling the issue *on observational grounds* of the detailed form of the MMR (and indeed whether or not it exists in all galaxies) is of some urgency because confusion over the form of the correlation has already arisen in the literature. Yet it is likely to bear quite directly on understanding the formation of massive GCs and their early star formation history (Harris et al. 2006; Mieske et al. 2006; Strader & Smith 2008; Bailin & Harris 2009).

In this paper I discuss new photometry of the M87 GCs obtained with CFHT/Megacam. The data com-

prise a large enough GC sample ($N \simeq 10^4$) to analyze the MMR to deep limits in addition to correlation with galactocentric distance. The sample size provides the obvious advantage that features such as the MMR, the spatial distribution, or the GCLF can be studied within a *single* galaxy without having to put together composite samples. The results discussed in the following sections show well defined blue and red GC sequences extending to high mass, and exhibit a nonlinear MMR quite similar to the ones in the six-galaxy BCG sample. Though M87 alone can hardly settle the question of the universality of the MMR, these results reinforce the need to investigate this intriguing effect further. In the present paper, I concentrate on the various features of the color and metallicity distributions.

In this discussion I adopt a distance modulus $(m - M)_0 = 31.0$ for M87 and the core of the Virgo cluster (Jerjen et al. 2004; Caldwell 2006; Williams et al. 2007) and a foreground absorption and reddening $A_I = 0.04$, $E_{V-I} = 0.03$. In the SDSS filter system the corresponding values relevant here are $A_i = 0.04$, $E_{g-i} = 0.04$, $E_{g-r} = 0.02$.

2. THE DATA SAMPLE

The 36 CCDs making up the CFHT Megacam array provide a 1° square field of view and the camera is normally used with the $u'g'r'i'z'$ filter set (in what follows I will drop the accents and refer to the magnitudes simply as *ugriz*). The image scale is $0.187''/\text{px}$ and the entire field makes up a $20\text{K} \times 20\text{K}$ array. The data used in this paper consist of a single set of homogeneous exposures centered on M87 taken in *gri* during 2004 March and April (Harris, PI), as listed in Table 1. While this material will eventually be surpassed by the much more extensive CFHT/Megacam Next-Generation Virgo Cluster Survey by Ferrarese et al. (see www.astrosci.ca/NGVS), much can already be extracted from the earlier set of M87-centered exposures.

Individual exposures in each filter were taken with a “small dither” pattern sufficient to splice over the small gaps between the individual CCDs in the array, but the much larger gaps between the top two ranks of CCDs and the bottom two ranks are still present (standard large-dither patterns are available for the camera that would cross these gaps, but these make the astrometric re-registration more difficult). These remaining gaps show up as two $\simeq 350$ -pixel-wide blank E/W stripes in the array, making up about 3.5% of its total area on the sky. The hour-long total exposure times in each filter were chosen to reach closely similar limiting absolute magnitudes for the globular clusters. The combined images in each filter are the ones produced through the Megapipe facility of CADC, and were downloaded from the CADC Archive ready for photometry.

The GCs around M87 are seen against a population of field objects including foreground Milky Way stars and background galaxies. Because the Virgo field is at high latitude, the contamination from stars is minimal and the main contaminants are small, faint galaxies. However, much of the field galaxy population can be removed by morphology because the GCs themselves appear starlike on these ground-based images. At the 16-Mpc distance of Virgo, an *average* GC half-light diameter of 5 pc (Harris 1996) is equivalent to $0.06''$, which in turn corresponds

¹ In this and most previous MMR work, the fundamental but well justified assumption is made that the spread of broadband optical color indices directly represents differences in metallicity, with $[\text{Fe}/\text{H}]$ increasing monotonically as the color index gets redder. The effects of other parameters on their broadband colors (such as cluster age or α -abundance) generate far more subtle changes in color. Convincing measurements of age or α differences between old GCs traditionally require careful analysis of high- S/N integrated spectra and are challenging to uncover even then; see, for example, Puzia et al. (2005); Peng et al. (2006); Strader et al. (2006); Pessev et al. (2008) among others, as well as comparisons of contemporary simple stellar population (SSP) models (e.g. Pessev et al. 2008).

to a FWHM of $0.04''$ for an average King-model concentration $\log(r_t/r_c) = 1.5$ (Larsen 1999). This scale size is thus 20 times smaller than the $0.8''$ FWHM seeing on the combined Megacam frames in this dataset, making any such objects indistinguishable from stars. Extensive quantitative tests of PSF-convolved globular cluster profiles for distant galaxies such as these show explicitly that the intrinsic profile width falls below the threshold of measurement if its FWHM is less than 10 percent of the PSF width (e.g. Larsen 1999; Harris 2009). In practice, what this means for the present data is that the GCs can be accurately measured either through conventional fixed-aperture or PSF-fitting photometry. Because the crowding levels are minimal, aperture photometry is adopted here (see below), with an aperture radius set at its optimal value similar to the PSF FWHM. Use of aperture photometry also alleviates concerns over minor changes in the PSF shape across the field.

As another basis of comparison, it is worth noting that imaging of the M87 clusters with *ground-based* image quality of $0.8''$ is almost exactly analogous to imaging clusters in the Coma galaxies at $d = 100$ Mpc with *HST* image quality of $0.1''$. Explicit tests of PSF-convolved GC profiles for the Coma galaxies (Harris et al. 2009) with deep HST data verify that the intrinsic sizes of the GCs are too small to affect their integrated magnitudes from either PSF-fitting or fixed-aperture photometry at levels larger than $\gtrsim 0.02$ mag. Even further, when these second-order magnitude corrections are differenced between two filters ($g-i$ or $g-r$ in this case), the effects of aperture size corrections on *color* are even smaller third-order ones that can be completely neglected. Similar comments apply to the ($C - T_1$) ground-based photometry of M87 and NGC 1399 by Forte et al. (2007) in which the seeing was $1.0'' - 1.6''$.

The first step in the photometry was to find candidate objects on all three master images and to eliminate the majority of nonstellar objects. The SExtractor code (Bertin & Arnouts 1996) was run to do this, and plots were generated of the SE effective radius and FWHM versus aperture magnitude, as shown in Figure 1. Objects falling outside the generous “stellar” boxes marked in the figures are either very bright, saturated stars; obviously nonstellar extended galaxies; or extremely faint objects, all of which could be eliminated from the detection lists.

Next, the SE-culled finding lists defined separately in g, r, i were compared, and any objects found on *all three* filters and coordinate-matched to within ± 1.5 px were kept for the final photometric measurement run. These matched objects were measured through *daophot* with an aperture radius of 3.5 px ($0.65''$, equivalent to a linear size of 50 pc at the distance of M87). Crowding in this high-latitude field is negligible, and comparisons of the fixed-aperture magnitudes with PSF-fitted magnitudes showed no differences in the resulting color-magnitude diagrams.

3. ASTROMETRIC AND PHOTOMETRIC CALIBRATION

The Megacam stacked images in the CADCE Archive have internally homogeneous astrometry that is already close to the most commonly used systems (such as SDSS, 2MASS, USNO), but to ensure that the data were on a specific astrometric system as closely as possible, the

USNO-B1 system was selected. The USNO-B1 catalog was searched for all objects within the Megacam field, and the positions of these objects were matched up with the (α, δ) values returned directly from the Megacam image headers. This matchup yielded 932 stars in common to within $1''$. Small zero-point offsets equal to $\Delta\alpha = (0.053 \pm 0.008)''$, $\Delta\delta = (0.254 \pm 0.008)''$ in the sense (USNO-CFHT) were found, but no significant higher-order terms. Figure 2 shows the residuals *after* the native Megacam astrometric coordinates were shifted onto the USNO-B1 system. The object-to-object rms scatter is $\pm 0.23''$ across the entire field, with no systematic deviations larger than $\pm 0.05''$.

The Megacam *ugriz* magnitudes are known to differ slightly from the Sloan Digital Sky Survey scales (see the Megacam webpages for updated calibration information). However, for the purposes of more direct comparison with other GCS data in the literature, it is useful to put the present M87 data onto the SDSS scale. The SDSS DR5 catalog was searched for objects in the M87 field and compared with the Megacam object lists, with the result that matches were found for about 1000 stars brighter than $i = 21.0$. These were used directly to set the photometric zero-points for *gri* in the M87 field. The mean differences $\Delta m = m(\text{CFHT}) - m(\text{SDSS})$ were found to be $\Delta(g) = 0.254 \pm 0.004$, $\Delta(r) = 0.407 \pm 0.008$, and $\Delta(i) = 0.412 \pm 0.006$, where the CFHT magnitudes are the ones defined simply using the zero-points in the image headers.

A secondary advantage of tying these data closely to a widely used standard system is that the intrinsic colors of globular clusters in the $(g-r)$ and $(g-i)$ indices have not previously been well established. The Virgo Cluster Survey data are in $(g-z)$ through the HST/ACS filters (Peng et al. 2006; Mieske et al. 2006). Previously published studies of GCSs for various galaxies in $(g-i)$ include Forbes et al. (2004), Wehner et al. (2008), and Cockcroft et al. (2009) all taken with Gemini/GMOS, but in all of these the absolute photometric calibrations are preliminary and not likely to be accurate to better than ± 0.1 mag (see these papers for detailed discussion). M87 offers an excellent opportunity to set up a fiducial color scale for GCs, not just because a direct matchup to the SDSS catalog is possible, but also because its foreground reddening is almost negligible and the statistical size of the GC population allows the mean colors of the red and blue sequences to be defined internally to ± 0.02 mag or better (see below).

4. DEFINITION OF THE GLOBULAR CLUSTER SYSTEM

In Figure 3 the final data for 20189 starlike or near-starlike objects are shown, plotted in $(i, g-r)$ and $(i, g-i)$. The detection rate for objects within the color range $(g-r) < 1.0$ is highly complete for $i < 23.5$; in the following analysis, the main conclusions rely even more conservatively on the interval $i < 23.0$ and are unaffected by any incompleteness.

Several clearly distinct components show up. The GCs that we are after lie on the two nearly vertical, narrow sequences at $(g-i) \simeq 0.8, 1.05$ while the populations bracketing these on the blue and red sides are the expected loci of foreground Milky Way halo and disk stars.

Any objects falling in the regions

$$\begin{aligned} (g-r) < 0.43, (g-r) > 0.95 \\ (g-i) < 0.59, (g-i) > 1.40 \\ i < 18.5 \end{aligned}$$

(the boundaries of which are marked by the boxes in Fig. 3) are thus rejected as field contamination. This final culling leaves 11946 objects that make up our final “best” GC candidate list.

The distribution of the GC candidate colors by spatial location is shown in Figure 4. Here, the projected distance R from the center of M87 is expressed in units of $R_{eff} = 1.58'$, the effective radius of the galaxy’s spheroid light. A well known though still striking feature of the M87 GC system is its huge radial extent: the clusters extend detectably beyond even $R \sim 150$ kpc or $20 R_{eff}$ (see next section). The first hints of its huge GCS halo were already evident in the wide-field starcount work of Harris & Smith (1976) and more clearly outlined with the CCD-based photometry of McLaughlin et al. (1994) and Tamura et al. (2006). For comparison, however, the V -magnitude data of McLaughlin et al. (1994) could be used to trace the GCS out only to the radial limits of their single-CCD field at $R(max) \simeq 8' \simeq 40$ kpc. Tamura et al. (2006) used a combination of four Subaru Suprime-Cam pointings in three colors (BVI) to make up a surveyed region of $136' \times 27'$, about the same total area as the single Megacam field but oriented along the E/W direction. M87 itself is in the SW corner of their westernmost SCam pointing, while another Virgo giant NGC 4552 is in their third field pointing.

An equally striking feature of the spatial distribution from Fig. 4 is the difference between the blue and red GC subpopulations. The red sequence virtually disappears into the general spread of field contamination for $R \gtrsim 6-8R_{eff}$ ($\sim 12'$ or 50 kpc) while the blue sequence continues detectably outward much further. Two other illustrations of this are shown in Figures 5 and 6. As a first approximation we define the blue GCs as those in the color interval $0.59 \leq (g-i) \leq 0.93$, and the red GCs as those in $0.93 < (g-i) \leq 1.40$. In Fig. 5, the spatial positions of each type are shown. Tamura et al. (2006) and Forte et al. (2007) find exactly the same phenomenon and these papers provide a more detailed discussion of the spatial distributions of each component. In Fig. 6, the CMDs in $(i, g-i)$ are displayed for five radial zones. Whereas the blue and red sequences are almost equally populated for the innermost zone $R < 3'$, the red sequence dies away more rapidly outward, leaving the blue sequence to dominate at large radii.

5. RADIAL STRUCTURE

The M87 GCS is so populous and extended that the level of background contamination (that is, the field contamination still present in the list of starlike objects, assumed constant across the field) is hard to determine precisely. The contamination is completely unimportant at small radii, but at the largest radii of the survey it determines the effective limit beyond which the GCS can be traced. We have no truly remote “control field” adjacent to M87 for measuring σ_b , and ultimately a definitive measurement of the background field level

and the outermost radial profile of the M87 GCS will have to await the still wider-field work from the Next-Generation Virgo Survey. For the present, the outer parts of the single Megacam field itself must be used to gauge σ_b . A reasonable estimate can be made by noting that for $R \gtrsim 12R_{eff}$, the areal density of *red* objects ($i \leq 23.0$ and $0.93 < (g-i) < 1.4$) is nearly uniform at $\sigma = 0.36$ arcmin $^{-2}$, accounting for the edges of the frame and the two blank stripes in the CCD array. The color range enclosing the blue GC sequence is narrower ($0.59 \leq (g-i) \leq 0.93$), so if the color distribution of the contaminants is roughly uniform over this range, the level of the blue background will be proportionately smaller, $\sigma_{bkdg}(blue) \simeq 0.26$ arcmin $^{-2}$, for the same magnitude range $i < 23.0$. (See also Harris 2009 for more extensive tests and discussion of the background color distribution in similar high-latitude fields.) Thus for the present purposes I adopt a total $\sigma_{bkdg} \simeq 0.6$ arcmin $^{-2}$, with a true external uncertainty likely to be near ± 0.1 arcmin $^{-2}$.

In the final list of GC candidates defined above, there are 8313 objects brighter than $i = 23.0$. Subtracting off the background, this leaves a total GC population $N_{GC} \simeq 6200 \pm 350$ brighter than $M_I \simeq -8.5$, which is about 0.2 mag brighter than the turnover (peak) point of the luminosity function.

The actual radial profile of both the blue and red GC subsystems can be quantified by tracing the projected surface density σ_{cl} directly as a function of radius. The observed number density of all the *candidate* GCs is by definition $\sigma = \sigma_{cl} + \sigma_b$. The resulting background-subtracted data for $i \leq 23.0$ are listed in Table 2 and shown in Figure 7. The columns in the Table give the inner and outer radii of each annulus, the mean radius, the calculated total number of clusters in the annular zone after background subtraction, and the density σ_{cl} . The conventional log/log form ($\log \sigma_{cl}$ vs. $\log R$) is shown in the left panel, indicating that both the blue and red components fall off progressively more steeply with increasing radius. A standard Hubble profile, which is a power law with a core radius R_0 ,

$$\sigma_{cl}(R) = \sigma_0 \left(1 + \frac{R}{R_0}\right)^{-a} \quad (1)$$

provides a reasonable fit to either component. Fits of this model to the data (shown in Fig. 7) for the blue GCs give ($\sigma_0 = 66$ arcmin $^{-2}$, $R_0 = 2.0'$, $a = -1.8$); while for the red GCs, ($\sigma_0 = 150$ arcmin $^{-2}$, $R_0 = 1.2'$, $a = -2.1$). These are equivalent to simple power laws $\sigma \sim R^{-n}$ where the exponent n steepens continuously with radius,

$$n(R) = a \frac{(R/R_0)}{\left(1 + \frac{R}{R_0}\right)}. \quad (2)$$

Both components also follow a deVaucouleurs-law form ($\log \sigma_{cl}$ vs. $R^{1/4}$) fairly well over their entire observed run. In this form the best-fit equations describing each one are

$$\begin{aligned} \log \sigma_{cl}(blue) &= (3.154 \pm 0.067) - (1.760 \pm 0.045)(R/R_{eff})^{1/4} \quad (3) \\ \log \sigma_{cl}(red) &= (3.874 \pm 0.054) - (2.439 \pm 0.037)(R/R_{eff})^{1/4} \quad (4) \end{aligned}$$

where again the σ 's are in units of arcmin $^{-2}$ and the slopes are normalized to the R_{eff} of the halo light.

(These lines should, however, not be extrapolated inward where the density distribution flattens off more strongly.) For comparison, Tamura et al. (2006) found slopes (-1.47 ± 0.03) (blue) and (-2.44 ± 0.06) (red). As they discuss more extensively, the integrated light of the M87 halo has a $R^{1/4}$ -law slope of -2.36 ± 0.09 , strongly suggesting that the more metal-rich GC population can be directly linked to the similarly metal-rich population of the field halo stars. Much other discussion of similar results from several other galaxies reinforcing this interpretation and connecting with their evolutionary histories can be found in Lee et al. (1998, 2008); Harris & Harris (2002); Bassino et al. (2006); Forte et al. (2007); Shin & Kawata (2009) among others, and will not be repeated here.

The behavior of the deVaucouleurs-type profile fit itself, near its outer edge, provides a useful consistency check of our adopted backgrounds σ_b (blue,red). If we have chosen the background nearly correctly, then the resulting σ_{cl} profile can plausibly be claimed (as is the case for most other elliptical galaxies) to follow a nearly straight line in the $\log \sigma_{cl}$ vs. $r^{1/4}$ plane all the way to the outer edge of the data. An overestimate of σ_b would cause the background-subtracted profile to drop suddenly and unrealistically to zero at the edge, whereas an underestimate would cause σ_{cl} to flatten off artificially at large radius. Neither one is the case (Figure 7b), so the choice of background levels appears to be self-consistent within their stated internal uncertainties.

The σ_{cl} data indicate that the blue GCs exist in detectable numbers out to at least $R = 28'$ or $\simeq 130$ kpc. A final check of the present results comes from comparison with Tamura et al. (2006), whose SCam data extend along a line towards NGC 4552 out to $120'$ (more than 500 kpc) from M87. They find the blue-sequence GCs to extend detectably to $R = 30'$ (see their Figures 5 and 7), and present a model fit to the combined M87/N4552 counts that suggests the M87 GCs could even extend to $100'$ and more. Clearly, we have not yet traced the full extent of this system.

6. METALLICITY GRADIENTS

A second-order feature of the radial color distributions (Fig. 4) is a progressive change in the mean color of both the red and blue GCs with radius: in other words, both components show a metallicity gradient. This feature is clearest for $R \lesssim 8R_{eff}$ or about 60 kpc; beyond that point, the red clusters are almost absent and the blue clusters show no significant change in mean color. For the region inward of $8R_{eff}$, power-law fits yield

$$\langle g-i \rangle(blue) = 0.813 - 0.025 \log(R/R_{eff}), \quad (5)$$

$$\langle g-i \rangle(red) = 1.095 - 0.035 \log(R/R_{eff}). \quad (6)$$

where both slopes are uncertain by 10 percent. The single-stellar-population models of Maraston (2005), which provide integrated color indices for a variety of broadband colors including the SDSS filters, show that $\Delta(g-i)/\Delta[Z/H] = 0.21 \pm 0.05$ over the metallicity range $[Z/H] \lesssim -0.2$ that covers most GCs. The color slopes then convert into metallicity gradients $Z \sim R^{-\gamma}$ where $\gamma = 0.12 \pm 0.02$ (blue) and 0.17 ± 0.03 (red).

Comparable data for the GCSs in several other large galaxies are now in the literature. Geisler et al. (1996)

found $\gamma = 0.15 \pm 0.03$ (blue), 0.12 ± 0.06 (red) in the other Virgo supergiant NGC 4472. Forte et al. (2001) found $\gamma \sim 0.2$ for the blue GCs in two Fornax ellipticals, NGC 1399 and 1427. Most recently, Harris (2009) derived a mean $\gamma = 0.10 \pm 0.02$ for both the blue and red GCs in six giant Brightest Cluster Galaxies. All these results are similar, and begin to present a very consistent picture: the mean GC metallicity in these large galaxies depends on spatial location, becoming more enriched the further inward it resides in the halo.

The widespread presence of metallicity gradients, albeit shallow, indicates that *both the major epochs of GC formation*, metal-poor and metal-rich, had a significant component of dissipative collapse of protogalactic gas and *in situ* formation which led to higher enrichment levels deeper in the potential wells of these large galaxies. Although gradients in the range $\gamma \sim 0.1-0.4$ for the dominant *metal-rich* field-star component have been found in many ellipticals within their central bulges ($R \lesssim R_{eff}$), the globular cluster data indicate that dissipative formation extended much further outward into their halos, to $\sim 5R_{eff}$ and beyond. What is perhaps equally important for understanding galaxy formation is that the *metal-poor* component, which is all but undetectable in the integrated field-star light, also has an inbuilt metallicity gradient to the same degree. This result makes it unlikely that the metal-poor stars all formed in pregalactic dwarfs that only later began to merge into bigger galaxies. Instead, the first major metal-poor round of star formation must have taken place while the initial stages of hierarchical merging were already underway (see Harris 2009, for further discussion and references)

7. BIMODAL SEQUENCE FITTING

We now look more closely at the blue and red GC sequences in the color-magnitude diagrams. The goal is to characterize each of the two sequences through their mean colors *as a function of magnitude* (the MMR) and their internal color (metallicity) dispersions. To define the MMR (or lack of one) we adopt the same basic approach as used in several previous studies (e.g. Harris et al. 2006; Mieske et al. 2006; Wehner et al. 2008; Bassino et al. 2008; Harris 2009, among others): the CMD is divided into narrow magnitude bins, and within each bin the color distribution of the GCs is fitted by a bimodal Gaussian model. Because each magnitude bin is treated independently, no *a priori* assumptions are made about the particular form of the MMR, whether linear or otherwise.

For the multimodal fitting, the code RMIX is used here (for extensive descriptions of RMIX applied to this situation, see Wehner et al. 2008; Harris 2009). The default approach – facilitated by the sheer statistical size of the M87 GC population – is to allow the code to solve freely for all five basic parameters in a Gaussian bimodal distribution: the mean colors of the two modes μ_1, μ_2 (blue, red), their dispersions σ_1, σ_2 (blue, red), and the relative numbers (proportions) p_1/p_2 of objects in each mode. The MMR along either of the sequences is then defined by any trend in the mean μ with magnitude.

The bimodal fits were done for objects within the zone $R < 6.5R_{eff}$, i.e. within the part of the M87 halo where both blue and red sequences are definitely present and in roughly equal numbers (Fig. 4). We restrict the sample

to objects in the color range $0.65 < (g-i) < 1.30$, and as a preliminary step, the shallow metallicity gradient described in the previous section is removed by normalizing the color indices to the values that all the clusters would have if they were at $R = R_{eff}$. That is, for the blue-sequence GCs (defined as those objects with $(g-i) < 0.95$), we define $(g-i)_{norm} = (g-i) + 0.0245 \log(R/R_{eff})$, and for the red-sequence GCs ($(g-i) > 0.95$), we define $(g-i)_{norm} = (g-i) + 0.0345 \log(R/R_{eff})$.

The results of these bimodal fits in both CMDs are summarized in Table 2, 3, and 4. Four separate runs were done with the following conditions, which were chosen to allow additional tests of the reality of any deduced MMR along both of the sequences:

- The data were divided into 0.25-magnitude bins in i , and within each bin all five free parameters ($\mu_1, \mu_2, \sigma_1, \sigma_2, p_1/p_2$) defining the bimodal Gaussian fit were freely determined by the fit (i.e., unconstrained). The exceptions to this were at the bright end, where for $i < 20.5$ half-magnitude bins were used to capture enough objects for a statistically significant fit. In addition, preliminary runs showed that for the four brightest bins ($i < 21.0$) the fully unconstrained fits tended to be unstable, so for these, the intrinsic widths of the two sequences were constrained to be equal to their average values on the lower bins, $\sigma_1 \equiv 0.060$ and $\sigma_2 \equiv 0.10$. The results for this run are summarized in Table 2. The columns list the i -magnitude range defining each bin; the number of objects in the bin; the best-fit blue-sequence parameters (μ_1, σ_1) and their uncertainties; the red-sequence parameters (μ_2, σ_2) and their uncertainties; and the best-fit proportion p_1 (the fraction of the total population belonging to the blue sequence). By definition $p_2 = 1 - p_1$.
- The same conditions as above were used, except that the *red* sequence was constrained to have a mean color $\mu_2 \equiv 1.070$, the average obtained from the lower-luminosity bins in the first (unconstrained) run. The color of the blue sequence was determined freely from the fit. The results for this run are summarized in Table 3.
- The same conditions were used, except that next the *blue* sequence was pinned at a mean color $\mu_1 \equiv 0.80$, the average obtained from the lower-luminosity bins in the first (unconstrained) run. The color of the red sequence was determined freely from the fit. The results for this run are summarized in Table 4.
- The mean colors of both sequences were pinned ($\mu_1 \equiv 0.80, \mu_2 \equiv 1.07$) and only the σ 's and proportions were solved for.

As an illustration of the overall quality of the fundamental assumption of bimodality, sample histogram fits for three representative magnitude ranges are shown in Figure 8. Two modes are definitely required, but the arbitrary addition of more than two subcomponents results in no formal improvement to the total color distribution (see also Larsen et al. 2001; Harris 2009; Cockcroft et al.

2009, for similar tests in several other galaxies), showing that bimodality is both a necessary and sufficient condition for describing the broadband-color distribution.

7.1. The Blue Sequence

The behavior of the key bimodal parameters (the means μ_1, μ_2 and the dispersions σ_1, σ_2) with luminosity is shown in Figure 9. A nonzero MMR will appear as a systematic trend of the mean color μ with magnitude. By using the bimodal fits to define the central colors of each mode, we also explicitly account for any overlap of the color distributions and possible asymmetric biasing due to contamination of one mode by the other. We concentrate first on the trends along the blue sequence, which to date is the only one of the two claimed to show a clear MMR, from the studies of many other galaxies.

The *blue sequence* in M87 shows up as a narrow, rather sharply defined feature in the CMD that is easily traced over the entire spatial region studied here. The narrow spread and large population on the blue sequence mean that the numerical solution for its position and shape is very stable. In the subsample used here for the fits, it takes up 55-60% of the total GC population, and the p_1 ratio stays nearly constant at all magnitude levels (upper panel of Figure 10).² Comparison of the results in Tables 2 and 3 (and displayed in Figure 9) shows that no significant changes in μ_1 or σ_1 occur when the red sequence is arbitrarily required to fall at a constant color. The mean color (normalized to $R = 1.0 R_{eff}$) is $(g-i)(blue) = 0.80 \pm 0.01$ over the fainter half of the i -magnitude range studied here. Its intrinsic width has a dispersion $\sigma_1 = 0.06 \pm 0.01$ that remains highly consistent with magnitude, except in the faintest range $i > 22.5$ where it is partially broadened by photometric measurement scatter. The Maraston (2005) population models used above then show that the dispersion in color corresponds to an intrinsic rms metallicity spread $\sigma(\text{Fe}/\text{H}) = 0.30 \pm 0.08$. For comparison, Harris (2009) found $\sigma(\text{Fe}/\text{H})(blue) = 0.27$ for the average of six other BCGs, measured from the $(B-I)$ color index.

The bimodal fits show that the blue sequence becomes smoothly and distinctly redder with increasing luminosity, especially for $i \lesssim 21.5$ ($M_I \lesssim -10$). Over this range, the mean color behaves as $(g-i)_{norm} = (0.845 \pm 0.090) - (0.021 \pm 0.004)(i - 20)$, a slope that is different from zero at the 5σ level. The resultant scaling of GC heavy-element abundance with luminosity is then $Z \sim L^{0.25 \pm 0.08}$. For comparison, Cockcroft et al. (2009) and Harris (2009) find an average blue-sequence scaling of $Z \sim L^{0.3 \pm 0.05}$ for more than a dozen large E galaxies measured from a variety of both ground-based and HST data and applying to a very similar GC luminosity range, though these studies also indicate that real differences from one galaxy to the next may exist.

At fainter levels ($M_I \gtrsim -10$, corresponding roughly to $10^6 M_\odot$), it is not clear that any significant trend exists and that the blue sequence could better be considered vertical. In summary, these results for M87 are closely

² This p_1 value is only a local one for the spatial region used here. The global one over the entire M87 halo will be larger because the blue GCs extend much further out into the halo. For comparison, Peng et al. (2008) find $p_1(\text{global}) = 0.73$ for M87 by integrating the number counts for both types of clusters to large radius.

similar to those of Harris (2009) for six other BCG giants: the MMR for the blue sequence in M87 exists, but it is nonlinear in form and most strongly affects the most massive clusters. Comparison of the Megacam result with the recent thorough analysis of the deep ($V - I$) data from HST/ACS (Peng et al. 2009) also shows close similarities: they found a clearly nonzero trend towards redder colors over the magnitude range $M_I \lesssim -9$ and a nearly vertical sequence below that.

The data discussed here emphasize that detecting the MMR correlation on observational grounds depends not just on using a metallicity-sensitive photometric index, but also on having a *very large sample that extends to high luminosity*. If we had restricted our analysis to just the inner zone (see, for example, the first panel of Figure 6), the MMR with its nonlinear form would be essentially undetectable. The Waters et al. (2009) study, which uses ($V - I$) colors for the clusters that fall in a single HST/ACS field, covers only the region within $2'$ of the center of M87. Their conclusion that no MMR is present in fact does not disagree with the present Megacam results for two reasons: first, at lower GC luminosity $M_I \gtrsim -10$ where the vast majority of the clusters fall, the MMR actually does become more nearly vertical and no trend is expected. Second, the smaller sample size in the HST/ACS data means that only a few dozen of its clusters lie above the transition level $M_I \sim -10$ where the MMR starts to become significant, making it hard to distinguish above the intrinsic scatter in the sequence. A more detailed comparative analysis of the HST/ACS data is provided by Peng et al. (2009).

7.2. The Red Sequence

The *red sequence* has a typical mean color $(g-i)_{norm} = 1.07$ averaged over all magnitudes, but it is less precisely definable at any level because its intrinsic dispersion $\sigma_2 \simeq 0.10 \pm 0.01$ is nearly twice as broad as that of the blue sequence. This larger spread also makes it more vulnerable to the field contamination at the upper end. The corresponding metallicity spread is $\sigma(\text{Fe}/\text{H}) = 0.50 \pm 0.13$. From their ($C - T_1$) photometry, Forte et al. (2007) measure a ratio $\sigma_1/\sigma_2 = 0.60$, in exact agreement with ours. For a combination of six other BCG galaxies, Harris (2009) found $\sigma(\text{Fe}/\text{H})(\text{red}) = 0.45$ from ($B - I$), also in good agreement with the M87 sequences.

In previous studies with other galaxies (notably Harris et al. 2006; Mieske et al. 2006; Harris 2009; Cockcroft et al. 2009; Peng et al. 2009, where explicit tests have been made) no significant MMR's have been claimed to exist along the red sequence. On theoretical grounds, if self-enrichment is the physical origin of the MMR then we do not expect to find any correlation of metallicity with mass along the red sequence *except* for extremely massive clusters (several million Solar masses and higher) where the amount of self-enrichment can finally reach above the already-large pre-enrichment level (see Bailin & Harris 2009). In most galaxies neither the blue nor red sequences reach that high. However, the large and homogeneous database for M87 offers a chance to test this notion empirically.

For the fainter range $i \gtrsim 21.5$, no significant change shows up in the mean color μ_2 . At brighter levels, the formal solutions show a surprisingly large change towards *bluer* mean color at higher luminosity; that is, the two se-

quences give the appearance of converging towards each other there. Taken at face value, the red sequence would then display a “negative MMR” towards lower metallicity at higher mass, contrary to any existing model interpretation. Nominally, the slope for the unconstrained fits in Table 2 is $\Delta(g-i)/\Delta i \simeq 0.03$, corresponding to $Z \sim L^{-(0.3 \pm 0.15)}$.

Closer examination indicates, however, that this trend is not as robust as for the blue sequence. Formally the slope is significant at only the $2 - \sigma$ level. Perhaps more importantly, the combined effects of its higher internal spread and the significant amount of field contamination in the CMD make the mean position of the sparsely populated upper end of the red sequence quite uncertain. This is shown in Table 4 and the upper panel of Figure 9. The numerical tests described above show that constraining the position of the *blue* sequence μ_1 has a large effect on the deduced position of μ_2 , pulling it much further to the blue. By contrast, the opposite test of constraining the red sequence color has no important effect on the blue sequence (lower pair of lines in Figure 9).

Another result of these tests is shown in the lower panel of Figure 10. Here, the ratio $\chi^2(\text{constrained})/\chi^2(\text{unconstrained})$ is plotted for the different sets of bimodal fits, to demonstrate what happens to the goodness-of-fit of each solution relative to the “baseline” model fit of Table 2. These χ^2 ratios are listed in the last columns of Tables 3 and 4. If we arbitrarily fix the red sequence (Table 3, and red line in Figure 10), then the quality of fit remains virtually as good as the baseline model except for the very brightest bin. But for the opposite case where we fix the blue sequence (Table 4, and blue line in Figure 10), a much more dramatic change occurs: at the bright end, the quality of fit degrades strongly. The same is true for the final set of fits where both sequences are arbitrarily constrained to their mean values. The case where the blue sequence is fixed also leads to a steep and unrealistic decrease in the p_1 ratio at the bright end (blue line in the upper panel of Figure 10).

In other words, over the range $i \gtrsim 21$ ($M_I \gtrsim -10.5$), the assumption that both sequences are strictly vertical (no MMR) provides an entirely reasonable fit to the data. Brighter than this, the null hypothesis of no MMR becomes increasingly invalid, and closer attention must be paid to the curvature in one or both of the sequences.

In summary, the present data point clearly to the existence of a blue-sequence MMR. Correctly representing it is crucial for the quality of fit of the entire color distribution. By contrast, the data indicate – though much more hesitantly – that a negative MMR may exist along the red sequence, though we cannot reject the null hypothesis (no MMR) as yet: the numerical tests described above show that ignoring the red MMR has very little effect on the quality of the bimodal fits.

The recent study of Peng et al. (2009) uses a sample of ~ 2000 M87 clusters measured in the less sensitive ($V - I$) color, but has the advantage that it is almost completely free of field contamination. They find that the red sequence has no significant slope at all luminosity levels.

8. DISCUSSION AND INTERPRETATION

The results of this study fall into line with the most complete recent collections of data for other large galaxies (Mieske et al. 2006; Harris 2009; Cockcroft et al. 2009). Above a transition point of about $10^6 M_\odot$, the low-metallicity clusters become progressively more enriched at higher luminosity, scaling as $Z \sim L^{0.25}$. This nonlinear MMR can be reasonably well understood through a basic self-enrichment model (Strader & Smith 2008; Bailin & Harris 2009).

At the same time, a MMR of similar amplitude and reverse direction – but of much lower significance – is found along the red sequence, $Z \sim L^{-(0.3 \pm 0.15)}$. Interestingly, Cockcroft et al. (2009) find a mean scaling $Z(\text{red sequence}) \sim L^{-(0.1 \pm 0.1)}$ for the average of 15 giant E galaxies, a result that is only marginally different from zero but at least points in the same direction as the M87 data. Thus it may be worth considering how the red sequence could have embedded in it some form of substructure appearing as a MMR of its own in a way that does *not* require self-enrichment.

To discuss the possibilities, we first ask what the essential differences are between the two modes. The blue, metal-poor clusters make up a narrow, well defined sequence that is replicated in very much the same way over and over in galaxies of all types, differing primarily just in their total numbers within different galaxies. Their mean metallicity $\langle \text{Fe}/\text{H} \rangle \simeq -1.4$ is only weakly correlated with galaxy mass and shows very much the same internal dispersion $\sigma(\text{Fe}/\text{H}) \simeq 0.3$ from one system to another (e.g. Burgarella et al. 2001; Strader et al. 2004; Brodie & Strader 2006; Peng et al. 2006). In addition, the blue GCs display a consistently old ~ 13 –Gy mean age with little internal age spread (e.g. Puzia et al. 2005; Brodie & Strader 2006; Beasley et al. 2008; Marin-Franch et al. 2009). Many lines of argument advanced in recent years have built up the view that the metal-poor GCs are likely to have formed in the first brief round of star formation within the “pregalactic dwarfs” that began their star formation just at the beginning of the major stage of hierarchical merging, and additional metal-poor GCs could have accreted later as part of their host dwarf satellites (see especially Searle & Zinn 1978; Harris & Pudritz 1994; Forbes et al. 1997; Côté et al. 1998; Burgarella et al. 2001; Beasley et al. 2002; Kravtsov & Gnedin 2005; Brodie & Strader 2006; Bekki et al. 2008, among many others). These small host dwarfs with their shallow potential wells and initially metal-poor gas could support only one major round of star formation and thus left behind metal-poor stars plus much unconverted gas.

By contrast, the red, metal-richer sequence is a more heterogeneous population that in some ways is harder to model in detail. Their mean metallicity $\langle \text{Fe}/\text{H} \rangle \simeq -0.4$ correlates weakly with host galaxy luminosity (Forbes et al. 1997; Strader et al. 2004; Brodie & Strader 2006). Both their metallicity distribution and spatial distribution within the halos of their galaxies as a whole are similar to the *field-star* population that has a broad, metal-rich MDF and makes up the bulk of a typical giant elliptical (Geisler et al. 1996; Harris & Harris 2002; Rhode & Zepf 2004; Forte et al. 2007). That is, the metal-rich GCs can reasonably be thought of as forming during the major stage of hierar-

chical merging that built most of the galaxy. Hierarchical models (e.g. Beasley et al. 2002, 2003) show that multiple “in situ” starbursts, major mergers, and accretions of gas-rich satellites would all have contributed to this stage. If this basic picture is correct, then the final population of metal-rich GCs would be expected to have a wide range of ages and metallicities, and more so in bigger galaxies that experienced more starbursts and merging events. Furthermore, the red-GC populations should also differ in detail from one galaxy to another depending on their individual merger and starburst histories.

On the observational side, the evidence points increasingly to the same view that the metal-rich GC “population” is actually a composite of objects with various ages, with its subcomponent MDFs heavily overlapped and thus of nearly similar mean metallicities (e.g. Puzia et al. 2005; Kundu et al. 2005; Brodie et al. 2005; Dirsch et al. 2005; Larsen et al. 2005; Brodie & Strader 2006; Cenarro et al. 2007; Goudfrooij et al. 2007; Beasley et al. 2008; Maybhate et al. 2009). Consistent with this view, both the relative numbers and luminosity functions of the red sequence differ noticeably from one galaxy to another, so that the high-luminosity end of the red GCLF does not extend to the same maximum even in galaxies with similar total GC populations. For example, in NGC 1399 the blue and red sequences have very similar “upper ends” while in M87 the blue sequence extends much higher (Forte et al. 2007); see also the difference between the Antlia giants NGC 3258 and 3268 (Bassino et al. 2008). By contrast with most other systems, in the Hydra and Coma supergiants NGC 3311 and NGC 4874 the red sequence is the one that extends to higher luminosity, up to cluster masses $\simeq 10^7 M_\odot$ and perhaps higher (Wehner et al. 2008; Harris et al. 2009). Observations of young, massive star clusters in present-day starburst galaxies (Larsen & Richtler 2000; Larsen 2009) also show that the cluster formation efficiency and the initial cluster mass function can vary with the total star formation rate.

These various pieces of evidence point to a way to understand, at least in principle, how we might obtain a red GC sequence with an observable mass/metallicity relation that could be *either* positive or negative. In the simplest such case, suppose that the metal-rich GCs comprise two main subpopulations that can be thought of as the products of the two biggest mergers or starbursts that assembled the main body of the galaxy. In addition, suppose that the earlier and slightly *less* metal-rich of these two starbursts generated its GCs with a broader mass function that extended to higher luminosity than did the later and metal-richer burst. What we would see today in the GCS as a whole would then be a red sequence with a broad MDF and a “negative MMR” at the top end. This population-based approach has nothing to do with any self-enrichment, is completely consistent with the evidence summarized above, and does not invoke any unusual physical effect. Simulated GCSs along these lines are now being constructed to test these ideas further and will be discussed in a later paper.

9. SUMMARY

Wide-field photometry with CFHT/Megacam in *gri* has been used to study the properties of the M87 globular cluster system. Approximately 6200 GCs have been

measured to a limit $i \simeq 23.0$ (equivalent roughly to $M_I \sim -8.5$, a little less than half the total population). The primary results of this study are these:

1. The metal-poor (blue) and metal-rich (red) cluster sequences are clearly delineated especially in the $(g - i)$ color index. While the red sequence does not extend detectably outward to projected galactocentric distances beyond ~ 50 kpc against the field contamination, the blue sequence can be seen to 100 kpc and beyond.
2. Both the red and blue subpopulations have shallow but significant radial metallicity gradients, corresponding to heavy-element abundance scaling with distance of $Z \sim R^{-0.12}$ (blue) and $Z \sim R^{-0.17}$ (red).
3. The blue sequence shows a nonlinear mass/metallicity relation: GC metallicity increases with luminosity. This relation is nearly vertical (that is, mean color is uncorrelated with metallicity) for $M_I \gtrsim -10$, while at brighter levels we find a trend roughly reproduced by $Z \sim L^{0.25}$. This result agrees well with the findings in numerous other giant E galaxies, as well as the best current data on M87 itself. Finding the trend depends critically on being able to sample the GC population to its highest luminosity levels. The blue-sequence MMR can be physically understood as the result of GC self-enrichment during formation.

4. The red sequence is almost twice as broad as the blue sequence in its internal scatter of colors. The formal numerical solutions show that it has a “negative MMR” at the top end that is at least as steep as the blue-sequence MMR. However, the same numerical solutions show that this trend is not strongly significant, and simply assuming a constant mean color for the red sequence does not noticeably decrease the quality of the bimodal fits.
5. In giant galaxies like M87, the red-GC sequence is likely to be a composite population, unlike the more internally homogeneous blue sequence. Every major starburst or gas-rich merger that contributed to the formation of the main body of the galaxy should have contributed to its metal-rich GC population. If the individual major starbursts generated GCs following slightly different initial mass functions, then features such as the negative-MMR can be built in to the total red sequence that we see today.

This work was supported by the Natural Sciences and Engineering Research Council of Canada through research grants to WEH, and by the Killam Foundation of the Canada Council through a research fellowship. It is a pleasure to acknowledge the Canadian Astronomy Data Center (CADK) and the high quality of their archive products that facilitated this study.

REFERENCES

- Bailin, J., & Harris, W.E. 2009, *ApJ*, 695, 1082
 Bassino, L.P., Faifer, F.R., Forte, J.C., Dirsch, B., Richtler, T., Geisler, D., & Schuberth, Y. 2006, *A&A*, 451, 789
 Bassino, L.P., Richtler, T., & Dirsch, B. 2008, *MNRAS*, 386, 1145
 Beasley, M., Baugh, C.M., Forbes, D.A., Sharples, R.M., & Frenk, C.S. 2002, *MNRAS*, 333, 383
 Beasley, M., Harris, W.E., Harris, G.L.H., & Forbes, D.A. 2003, *MNRAS*, 340, 341
 Beasley, M., Bridges, T., Peng, E., Harris, W.E., Harris, G.L.H., Forbes, D.A., & Mackie, G. 2008, *MNRAS*, 386, 1443
 Bekki, K., Yahagi, H., Nagashima, M., & Forbes, D.A. 2008, *MNRAS*, 387, 1131
 Bertin, E., & Arnouts, S. 1996, *A&AS*, 117, 393
 Brodie, J.P., & Strader, J. 2006, *ARA&A*, 44, 193
 Brodie, J.P., Strader, J., Denicol, G., Beasley, M.A., Cenarro, A.J., Larsen, S.S., Kuntschner, H., & Forbes, D.A. 2005, *AJ*, 129, 2643
 Burgarella, D., Kissler-Patig, M., & Buat, V. 2001, *AJ*, 121, 2647
 Caldwell, N. 2006, *ApJ*, 651, 822
 Carter, D., & Dixon, K.L. 1978, *AJ*, 83, 574
 Cenarro, A.J., Beasley, M.A., Strader, J., Brodie, J.P., & Forbes, D.A. 2007, *AJ*, 134, 391
 Cockcroft, R., Harris, W.E., Wehner, E.M.H., Whitmore, B.C., & Rothberg, B. 2009, *AJ*, in press (arXiv:0906:2008)
 Cohen, J.G. 1986, *AJ*, 92, 1039
 Côté, P., Marzke, R.O., & West, M.J. 1998, *ApJ*, 501, 554
 Côté, P. et al. 2004, *ApJS*, 153, 223
 Dirsch, B., Schuberth, Y., & Richtler, T. 2005, *A&A*, 433, 43
 Forbes, D.A., Brodie, J.P., & Grillmair, C.J. 1997, *AJ*, 113, 1652
 Forbes, D.A., Faifer, F.R., Forte, J.C., Bridges, T., Beasley, M.A., Gebhardt, K., Hanes, D.A., Sharples, R., & Zepf, S.E. 2004, *MNRAS*, 355, 608
 Forte, J.C., Faifer, F., & Geisler, D. 2007, *MNRAS*, 382, 1947
 Forte, J.C., Geisler, D., Ostrov, P.G., Piatti, A.E., & Gieren, W. 2001, *AJ*, 121, 1992
 Geisler, D., Lee, M.G., & Kim, E. 1996, *AJ*, 111, 1529
 Goudfrooij, P., Schweizer, F., Gilmore, D., & Whitmore, B.C. 2007, *AJ*, 133, 2737
 Grillmair, C., Pritchett, C., & van den Bergh, S. 1986, *AJ*, 91, 1328
 Harris, W.E. 1996, *AJ*, 112, 1487
 Harris, W.E., Whitmore, B.C., Karakla, D., Okon, W., Baum, W.A., Hanes, D.A., & Kavelaars, J.J. 2006, *ApJ*, 636, 90
 Harris, W.E. 2009, *ApJ*, submitted
 Harris, W.E., & Harris, G.L.H. 2002, *AJ*, 123, 3108
 Harris, W.E., Kavelaars, J.J., Hanes, D.A., Pritchett, C.J., & Baum, W.A. 2009, *AJ*, 137, 3314
 Harris, W.E., & Pudritz, R.E. 1994, *ApJ*, 429, 177
 Harris, W.E., & Smith, M.G. 1976, *ApJ*, 207, 1036
 Ivezić, Z. et al. 2007, *AJ*, 134, 973
 Jerjen, H., Binggeli, B., & Barazza, F.D. 2004, *AJ*, 127, 771
 Jordán, A., Peng, E.W., Blakeslee, J.P., Côté, P., Eyheramendy, S., Ferrarese, L., Mei, S., Tonry, J.L., & West, M.J. 2009, *ApJS*, 180, 54
 King, I.R. 1978, *ApJ*, 222, 1
 Kravtsov, A.V., & Gnedin, O.Y. 2005, *ApJ*, 623, 650
 Kundu, A. et al. 2005, *ApJ*, 634, L41
 Larsen, S.S. 1999, *A&AS*, 139, 393
 Larsen, S.S. 2009, *A&A*, 494, 539
 Larsen, S.S., Brodie, J.P., Huchra, J.P., Forbes, D.A., & Grillmair, C.J. 2001, *AJ*, 121, 2974
 Larsen, S.S., Brodie, J.P., & Strader, J. 2005, *A&A*, 443, 413
 Larsen, S.S., & Richtler, T. 2000, *A&A*, 354, 836
 Lee, M.G., Kim, E., & Geisler, D. 1998, *AJ*, 115, 947
 Lee, M.G., Park, H.S., Kim, E., Hwang, H.S., Kim, S.C., & Geisler, D. 2008, *ApJ*, 682, 135
 Liu, Y., Zhou, X., Ma, J., Wu, H., Yang, Y., Li, J., & Chen, J. 2005, *AJ*, 129, 2628
 Maraston, C. 2005, *MNRAS*, 362, 799
 Marin-Franch, A. et al. 2009, *ApJ*, 694, 1498
 Maybhate, A., Goudfrooij, P., Schweizer, F., Puzia, T.H., & Carter, D. 2009, *AJ*, 137, 383
 McLaughlin, D.E., Harris, W.E., & Hanes, D.A. 1994, *ApJ*, 422, 486
 McLaughlin, D.E., Secker, J., & Harris, W.E. 1995, *AJ*, 109, 1033
 Mieske, S. et al. 2006, *ApJ*, 653, 193
 Peletier, R.F., Davies, R.L., Illingworth, G.D., Davis, L.E., & Cawson, M. *AJ*, 100, 1091
 Peng, E.W. et al., 2006, *ApJ*, 639, 95
 Peng, E.W. et al., 2008, *ApJ*, 681, 197

- Peng, E.W., Jordán, A., Blakeslee, J.P., Mieske, S., Côté, P., Ferrarese, L., Harris, W.E., Madrid, J.P., & Meurer, G. 2009, submitted for publication
- Peshev, P.M., Goudfrooij, P., Puzia, T.H., & Chandar, R. 2008, MNRAS, 385, 1535
- Puzia, T.H., Kissler-Patig, M., Thomas, D., Maraston, C., Saglia, R.P., Bender, R., Goudfrooij, P., & Hempel, M. 2005, A&A, 439, 997
- Rhode, K.L., & Zepf, S.E. 2004, AJ, 127, 302
- Searle, L., & Zinn, R. 1978, ApJ, 225, 357
- Shin, M.-S., & Kawata, D. 2009, ApJ, 691, 83
- Spitler, L.R., Larsen, S.S., Strader, J., Brodie, J.P., Forbes, D.A., & Beasley, M.A. 2006, AJ, 132, 1593
- Strader, J., Brodie, J.P., & Forbes, D.A. 2004, AJ, 127, 3431
- Strader, J., Brodie, J.P., Spitler, L., & Beasley, M.A. 2006, AJ, 132, 2333
- Strader, J., & Smith, G.H. 2008, AJ, 136, 1828
- Tamura, N., Sharples, R.M., Arimoto, N., Onodera, M., Ohta, K., & Yamada, Y. 2006, MNRAS, 373, 588
- Waters, C.Z., Zepf, S.E., Lauer, T.R., Baltz, E.A., & Silk, J. 2006, ApJ, 650, 885
- Waters, C.Z., Zepf, S.E., Lauer, T.R., & Baltz, E.A. 2009, ApJ, 693, 463
- Wehner, E.M.H., Harris, W.E., Whitmore, B.C., Rothberg, B., & Woodley, K.A. 2008, ApJ, 681, 1233
- Williams, B.F. et al. 2007, ApJ, 656, 756

TABLE 1
CFHT/MEGACAM IMAGES

Filter	$N(\text{exp})$	Total t (sec)	FWHM
g'	11	3520	$0.74''$
r'	10	3000	$0.80''$
i'	11	3300	$0.82''$

TABLE 2
RADIAL DISTRIBUTIONS

R Range	R	n_{cl}	σ_{cl} (arcmin $^{-2}$)
Blue GCs			
1.00' – 1.30'	1.14'	68.4	31.57 ± 3.83
1.30 – 1.69	1.48	84.1	22.94 ± 2.52
1.69 – 2.20	1.93	128.4	20.75 ± 1.84
2.20 – 2.86	2.50	135.3	12.93 ± 1.13
2.86 – 3.71	3.26	206.4	11.67 ± 0.83
3.71 – 4.83	4.23	256.2	8.57 ± 0.55
4.83 – 6.27	5.50	293.9	5.82 ± 0.36
6.27 – 8.16	7.15	388.8	4.56 ± 0.26
8.16 – 10.60	9.30	428.5	2.97 ± 0.18
10.60 – 13.79	12.09	423.6	1.74 ± 0.14
13.79 – 17.92	15.72	426.8	1.04 ± 0.12
17.92 – 23.30	20.43	472.9	0.68 ± 0.11
23.30 – 30.29	26.56	382.1	0.33 ± 0.10
Red GCs			
1.00' – 1.30'	1.14'	81.2	37.47 ± 4.18
1.30 – 1.69	1.48	102.7	28.03 ± 2.79
1.69 – 2.20	1.93	135.8	21.93 ± 1.90
2.20 – 2.86	2.50	143.2	13.69 ± 1.16
2.86 – 3.71	3.26	167.6	9.48 ± 0.75
3.71 – 4.83	4.23	170.2	5.70 ± 0.46
4.83 – 6.27	5.50	186.8	3.70 ± 0.30
6.27 – 8.16	7.15	189.3	2.22 ± 0.20
8.16 – 10.60	9.30	187.1	1.30 ± 0.15
10.60 – 13.79	12.09	166.2	0.68 ± 0.12
13.79 – 17.92	15.72	145.7	0.35 ± 0.11
17.92 – 23.30	20.43	94.4	0.14 ± 0.10

TABLE 3
RMIX BIMODAL FITS TO THE $(g - i)$ COLORS

i range	$N(\text{bin})$	$\mu_1 (\pm)$	$\sigma_1 (\pm)$	$\mu_2 (\pm)$	$\sigma_2 (\pm)$	$p_1 (\pm)$
(23.00, 23.25)	455	0.809(0.009)	0.085(0.007)	1.097(0.018)	0.099(0.013)	0.633(0.035)
(22.75, 23.00)	497	0.798(0.008)	0.079(0.006)	1.097(0.013)	0.092(0.010)	0.616(0.035)
(22.50, 22.75)	486	0.799(0.006)	0.064(0.004)	1.078(0.013)	0.100(0.009)	0.576(0.035)
(22.25, 22.50)	397	0.790(0.007)	0.066(0.006)	1.079(0.017)	0.116(0.013)	0.542(0.035)
(22.00, 22.25)	330	0.807(0.007)	0.064(0.005)	1.083(0.013)	0.086(0.010)	0.606(0.035)
(21.75, 22.00)	311	0.802(0.006)	0.059(0.005)	1.077(0.013)	0.098(0.010)	0.553(0.035)
(21.50, 21.75)	257	0.806(0.008)	0.061(0.006)	1.073(0.022)	0.105(0.015)	0.592(0.035)
(21.25, 21.50)	191	0.818(0.012)	0.068(0.008)	1.067(0.030)	0.095(0.019)	0.625(0.035)
(21.00, 21.25)	152	0.829(0.010)	0.052(0.011)	0.996(0.040)	0.122(0.019)	0.415(0.035)
(20.75, 21.00)	138	0.838(0.009)	0.060(0.000)	1.051(0.020)	0.100(0.000)	0.591(0.058)
(20.50, 20.75)	115	0.823(0.009)	0.060(0.000)	1.026(0.021)	0.100(0.000)	0.586(0.064)
(20.00, 20.50)	122	0.846(0.010)	0.060(0.000)	1.033(0.021)	0.100(0.000)	0.540(0.072)
(19.50, 20.00)	57	0.844(0.017)	0.060(0.000)	0.985(0.033)	0.100(0.000)	0.466(0.143)

TABLE 4
BIMODAL FITS (RED SEQUENCE CONSTRAINED)

i range	$N(\text{bin})$	$\mu_1 (\pm)$	$\sigma_1 (\pm)$	$\sigma_2 (\pm)$	$p_1 (\pm)$	$\chi^2_{\nu}(\text{con})/\chi^2_{\nu}(\text{uncon})$
(23.00, 23.25)	455	0.799(0.009)	0.079(0.005)	0.114(0.009)	0.578(0.030)	1.08
(22.75, 23.00)	497	0.788(0.006)	0.072(0.005)	0.108(0.007)	0.562(0.028)	1.11
(22.50, 22.75)	486	0.797(0.005)	0.062(0.004)	0.104(0.007)	0.562(0.027)	0.90
(22.25, 22.50)	397	0.787(0.006)	0.064(0.005)	0.121(0.009)	0.527(0.031)	0.92
(22.00, 22.25)	330	0.803(0.006)	0.061(0.004)	0.093(0.008)	0.582(0.032)	0.91
(21.75, 22.00)	311	0.800(0.005)	0.057(0.004)	0.102(0.008)	0.542(0.033)	0.92
(21.50, 21.75)	257	0.805(0.006)	0.060(0.005)	0.106(0.010)	0.587(0.038)	0.88
(21.25, 21.50)	191	0.819(0.008)	0.068(0.006)	0.093(0.011)	0.631(0.043)	0.88
(21.00, 21.25)	152	0.848(0.010)	0.068(0.008)	0.094(0.013)	0.676(0.056)	1.11
(20.75, 21.00)	138	0.841(0.008)	0.060(0.000)	0.100(0.000)	0.618(0.048)	0.99
(20.50, 20.75)	115	0.829(0.008)	0.060(0.000)	0.100(0.000)	0.640(0.051)	1.13
(20.00, 20.50)	122	0.853(0.009)	0.060(0.000)	0.100(0.000)	0.605(0.054)	1.25
(19.50, 20.00)	57	0.871(0.011)	0.060(0.000)	0.100(0.000)	0.775(0.074)	1.82

TABLE 5
BIMODAL FITS (BLUE SEQUENCE CONSTRAINED)

i range	$N(\text{bin})$	$\sigma_1 (\pm)$	$\mu_2 (\pm)$	$\sigma_2 (\pm)$	$p_1 (\pm)$	$\chi^2_{\nu}(\text{con})/\chi^2_{\nu}(\text{uncon})$
(23.00, 23.25)	455	0.081(0.005)	1.083(0.014)	0.108(0.011)	0.600(0.034)	0.98
(22.75, 23.00)	497	0.080(0.005)	1.100(0.010)	0.090(0.008)	0.621(0.027)	0.88
(22.50, 22.75)	486	0.064(0.004)	1.079(0.010)	0.099(0.008)	0.579(0.028)	0.88
(22.25, 22.50)	397	0.071(0.005)	1.092(0.012)	0.107(0.009)	0.575(0.031)	1.22
(22.00, 22.25)	330	0.061(0.005)	1.074(0.012)	0.093(0.009)	0.582(0.035)	0.92
(21.75, 22.00)	311	0.058(0.004)	1.076(0.012)	0.099(0.009)	0.549(0.034)	0.88
(21.50, 21.75)	257	0.058(0.005)	1.063(0.018)	0.111(0.013)	0.569(0.044)	0.91
(21.25, 21.50)	191	0.059(0.007)	1.023(0.027)	0.119(0.017)	0.506(0.074)	0.98
(21.00, 21.25)	152	0.042(0.009)	0.965(0.019)	0.123(0.010)	0.301(0.083)	1.36
(20.75, 21.00)	138	0.060(0.000)	1.011(0.017)	0.100(0.000)	0.451(0.061)	1.49
(20.50, 20.75)	115	0.060(0.000)	1.004(0.020)	0.100(0.000)	0.513(0.066)	1.16
(20.00, 20.50)	122	0.060(0.000)	0.990(0.018)	0.100(0.000)	0.347(0.076)	6.83
(19.50, 20.00)	57	0.060(0.000)	0.918(0.028)	0.100(0.000)	0.063(0.206)	1.83

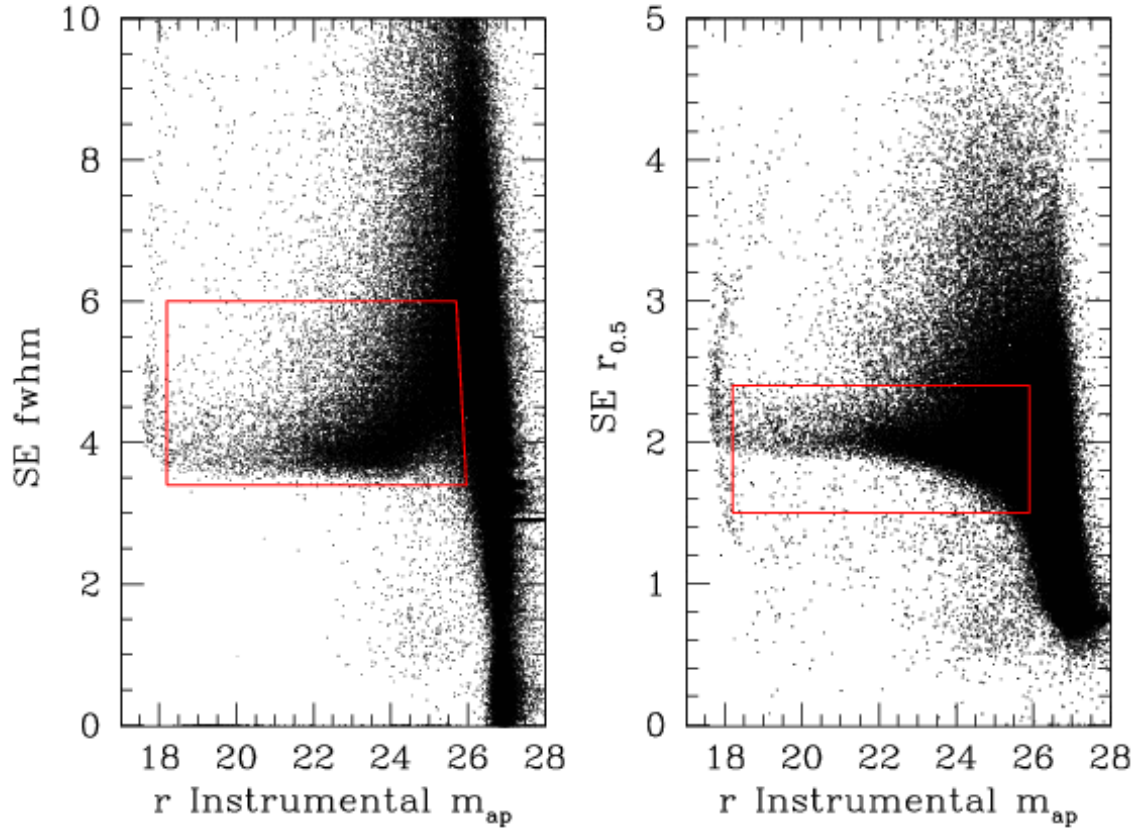


FIG. 1.— Use of SExtractor parameters for rejection of nonstellar objects. The measured FWHM and effective radius of each detected object on the M87 field are plotted against aperture magnitude. Objects lying outside either of the marked boxes are rejected from the detection lists (see text). The example shown here is from the r -band frame; note that the r values plotted here are only the raw instrumental magnitudes and should not be compared with the final color-magnitude diagrams below.

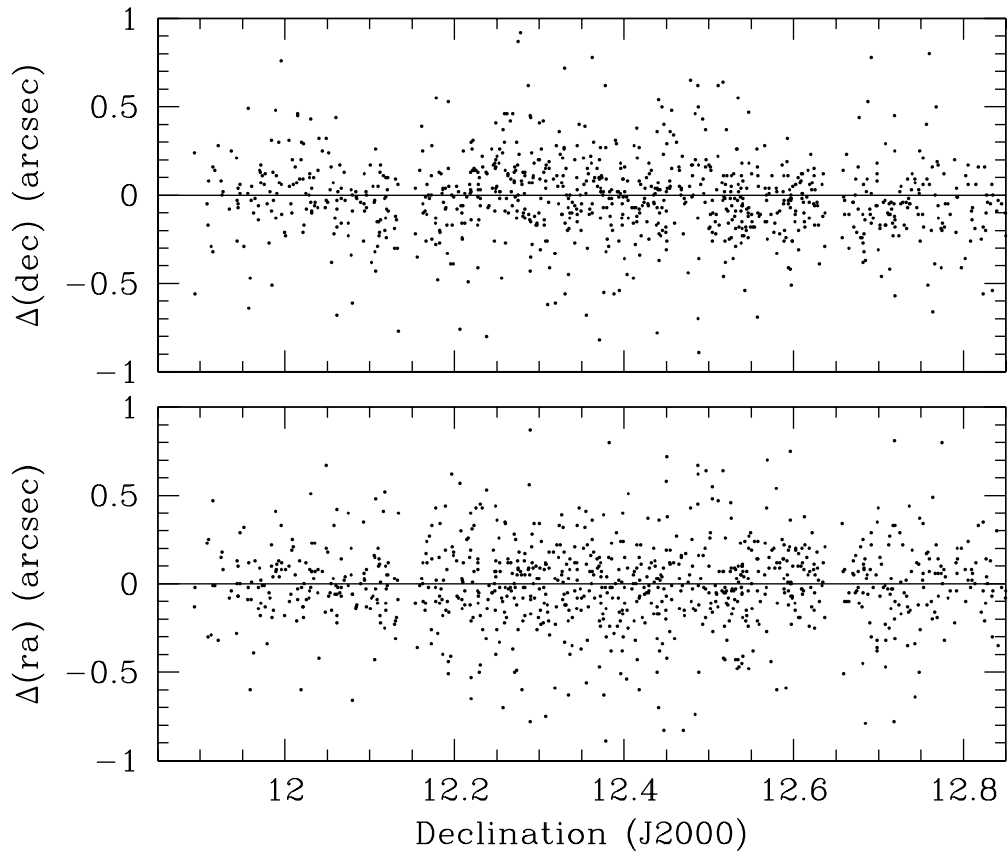


FIG. 2.— Residuals in the measured positions for the 932 stars in the USNO-B1 catalog that were found to lie within the M87 Megacam field, plotted as a function of declination in degrees. The rms scatter around zero is $\pm 0.23''$ in both right ascension and declination.

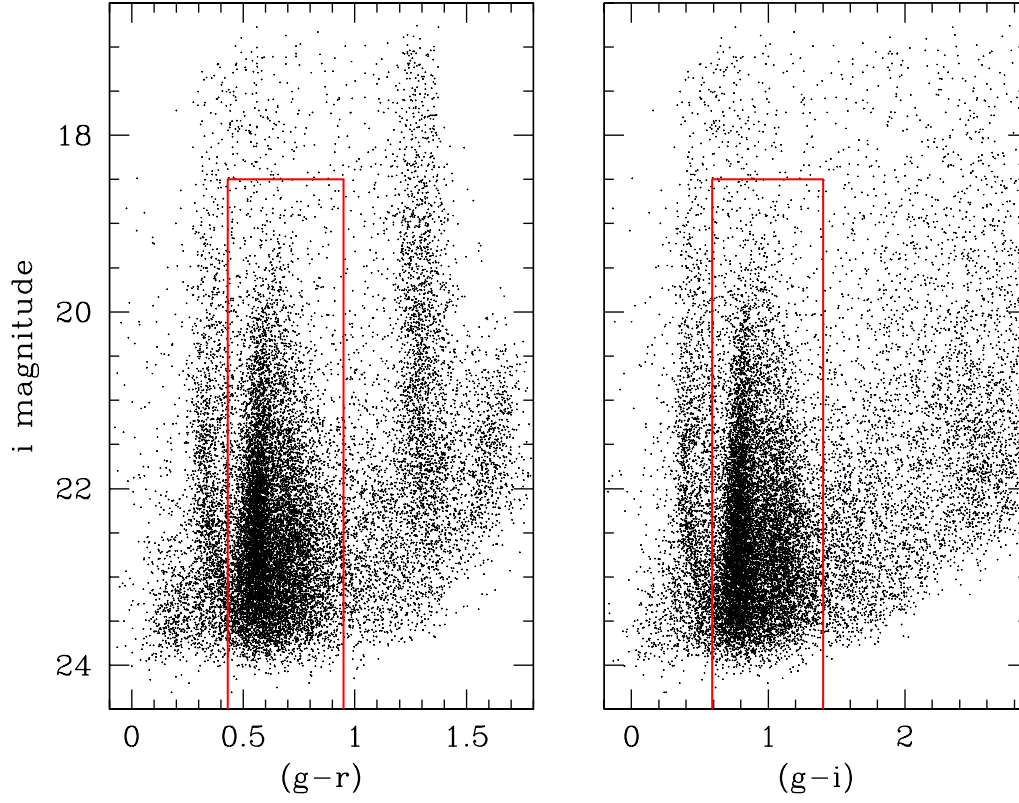


FIG. 3.— Final color-magnitude diagrams for the starlike and near-starlike objects detected in all three frames (g, r, i). Objects lying outside either of the marked boxes are rejected as field contamination (mostly foreground Milky Way halo or disk stars).

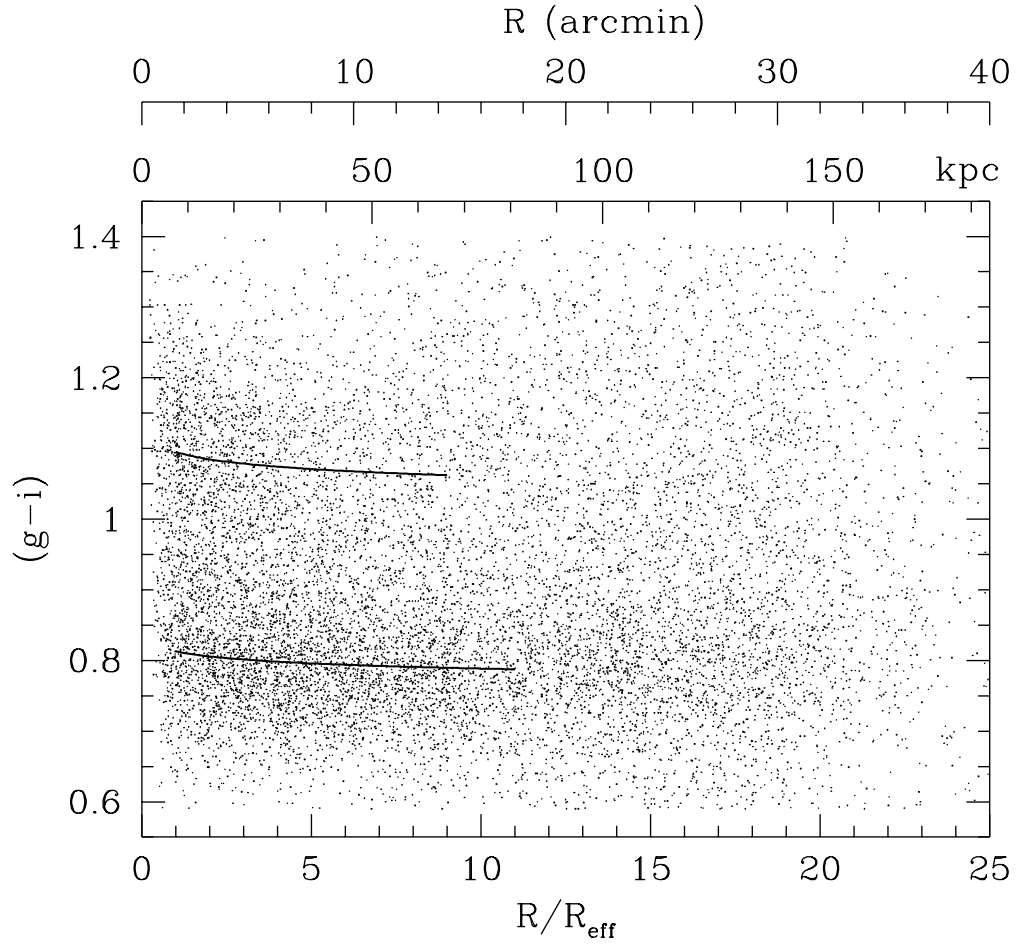


FIG. 4.— Measured $(g - i)$ color index versus projected galactocentric distance for the “starlike” objects brighter than $i = 23.0$. This sample is dominated by globular clusters (see text). Radii are plotted in units of the M87 spheroid effective radius (bottom axis) or in kiloparsecs or arcminutes (top axes). The calculated radial metallicity gradients for the blue and red GC sequences are shown by the solid lines.

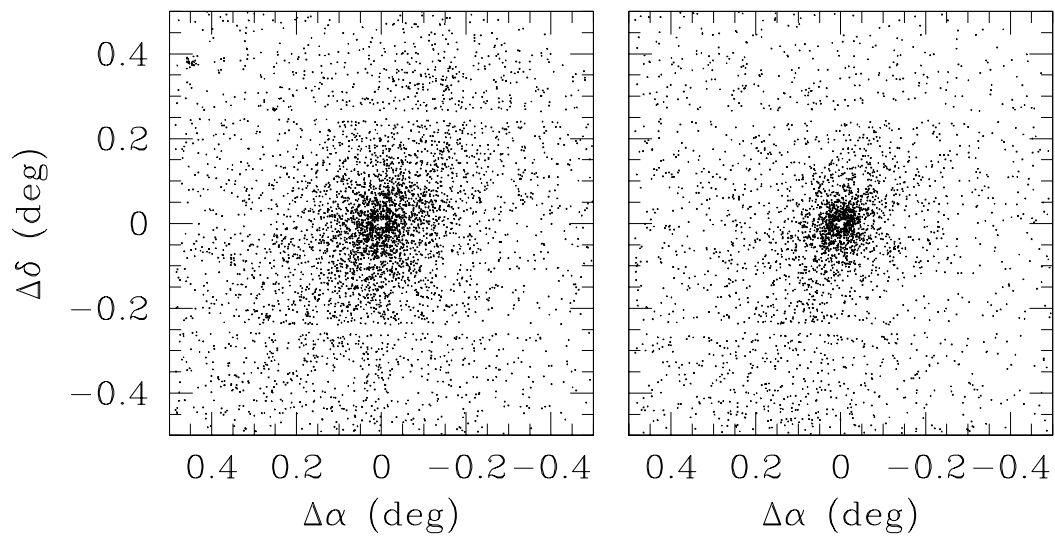


FIG. 5.— Spatial distributions of GC candidate objects brighter than $i = 23.0$ as in the previous figure, subdivided into the blue sequence (left panel) and red sequence (right panel). The much larger spatial extent of the blue GC population is evident. Note also the two vacant horizontal stripes above and below center that represent the large gaps between the ranks of CCDs in the camera mosaic.

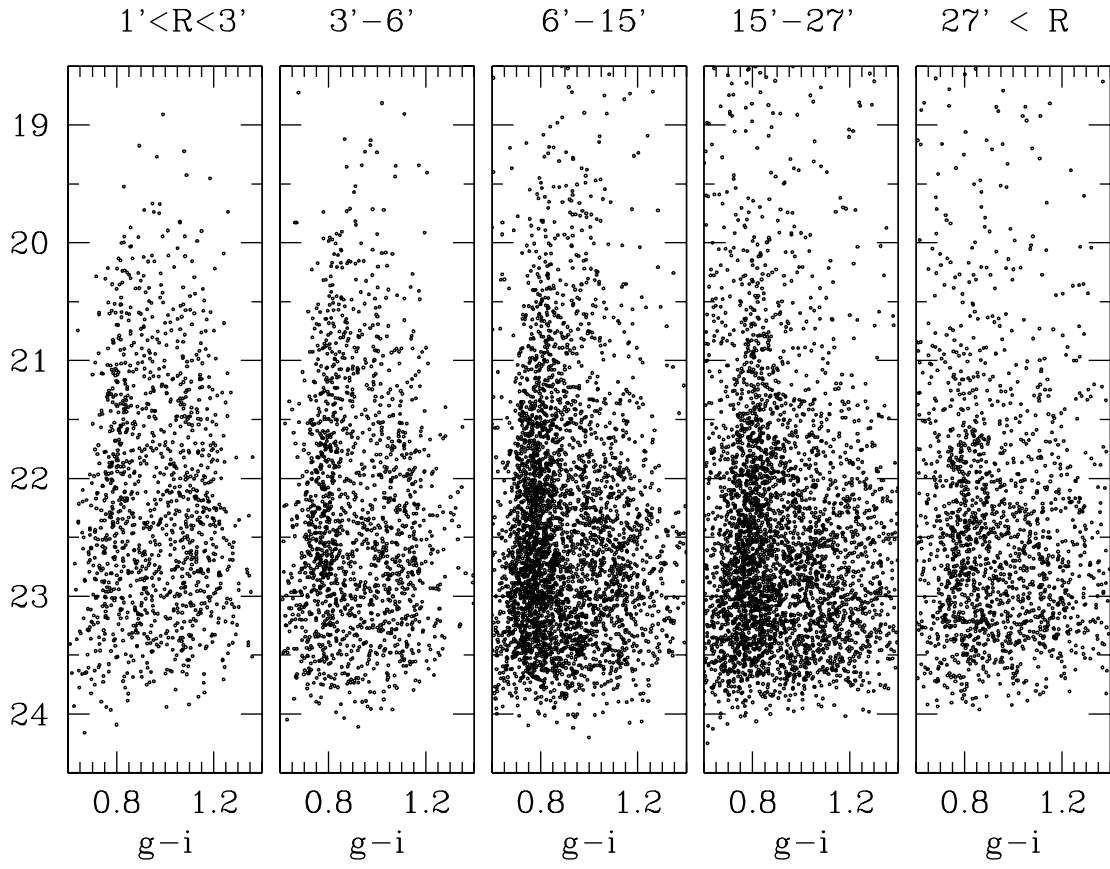


FIG. 6.— Color-magnitude data in $(i, g-i)$ for the starlike objects, separated by radial zone in projected galactocentric distance R . Five zones are shown.

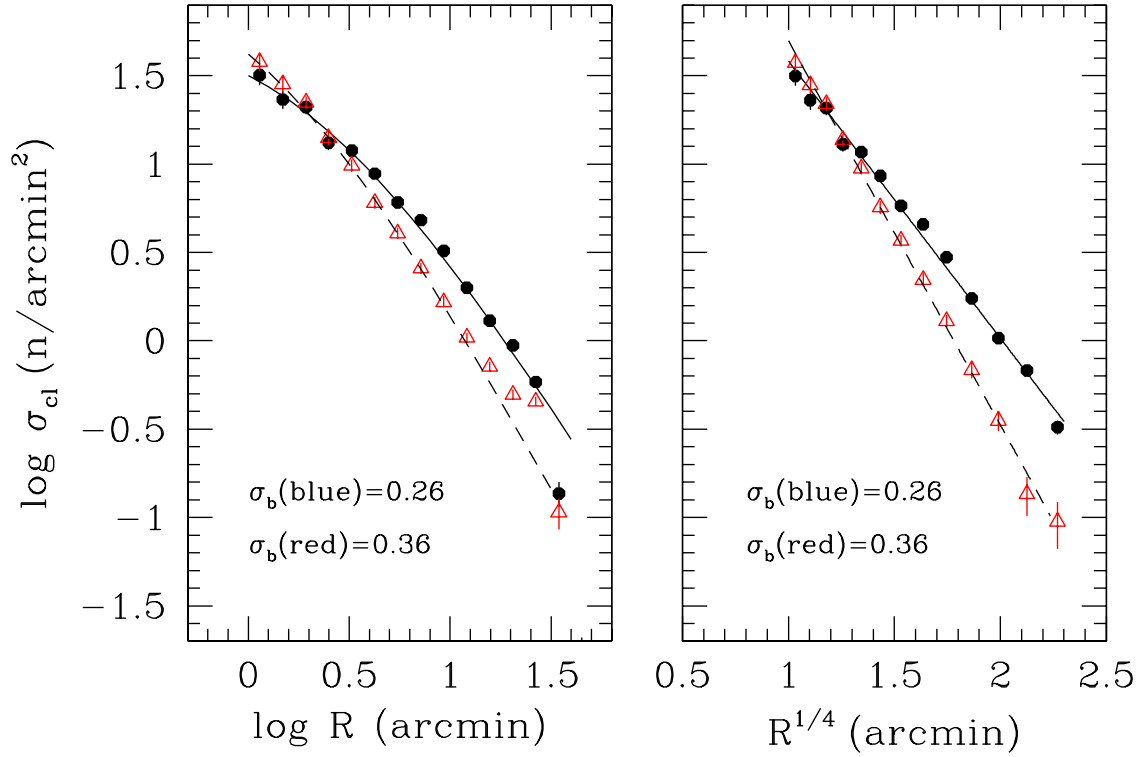


FIG. 7.— Projected radial profiles for the blue and red GC subsystems, using the $i < 23.0$ data from Figure 4. The number density of GCs, $\sigma_{cl} = \sigma - \sigma_{bkgd}$, is plotted in power-law form (left panel) and again in the de Vaucouleurs-law form (right panel). The blue-sequence GCs are shown as solid dots and the red-sequence GCs as open triangles. In the left panel the Hubble profiles fitting each of the two components as given in the text are superimposed.

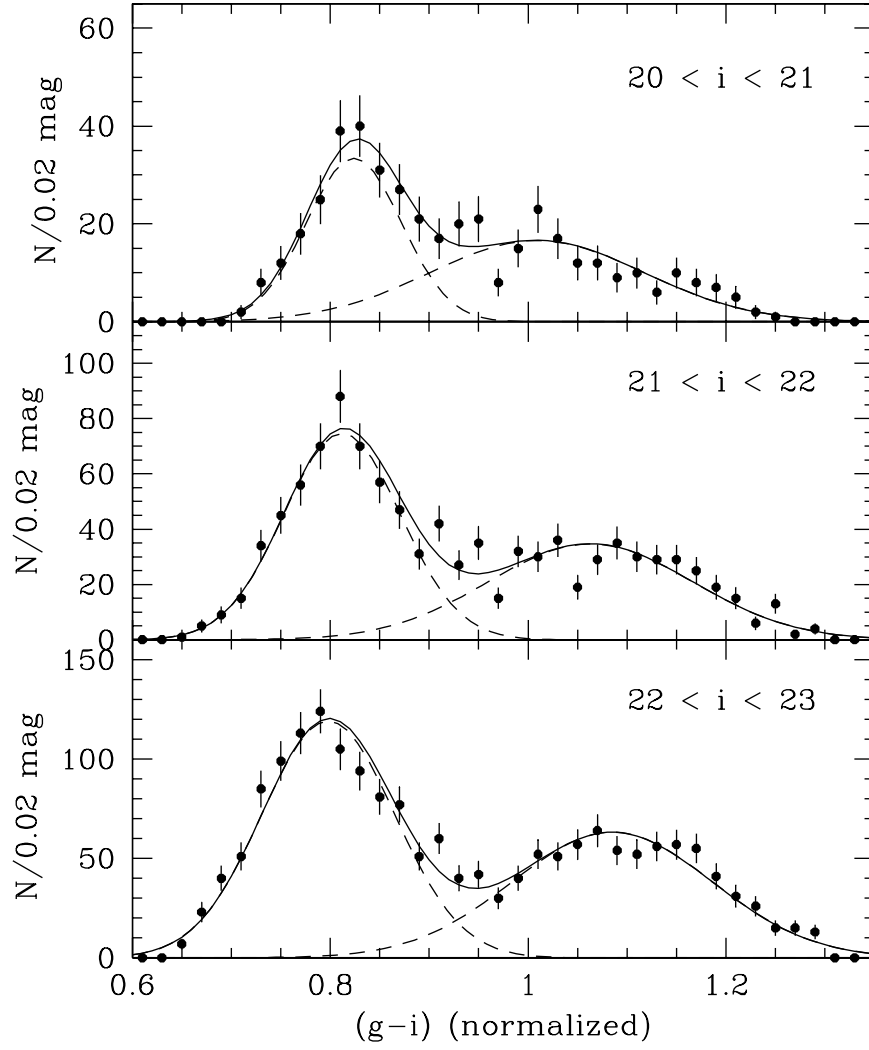


FIG. 8.— Sample RMIX solutions for the $(g-i)$ color distributions in three one-magnitude bins in i as labelled. The $(g-i)$ colors of the individual clusters are normalized to a galactocentric distance $R = 1.0R_{eff}$ to remove the spatial metallicity gradients in the system (see text). In each panel, the dashed lines show the Gaussian curves matching the blue and red sequences, while the solid lines show the sum of the two components.

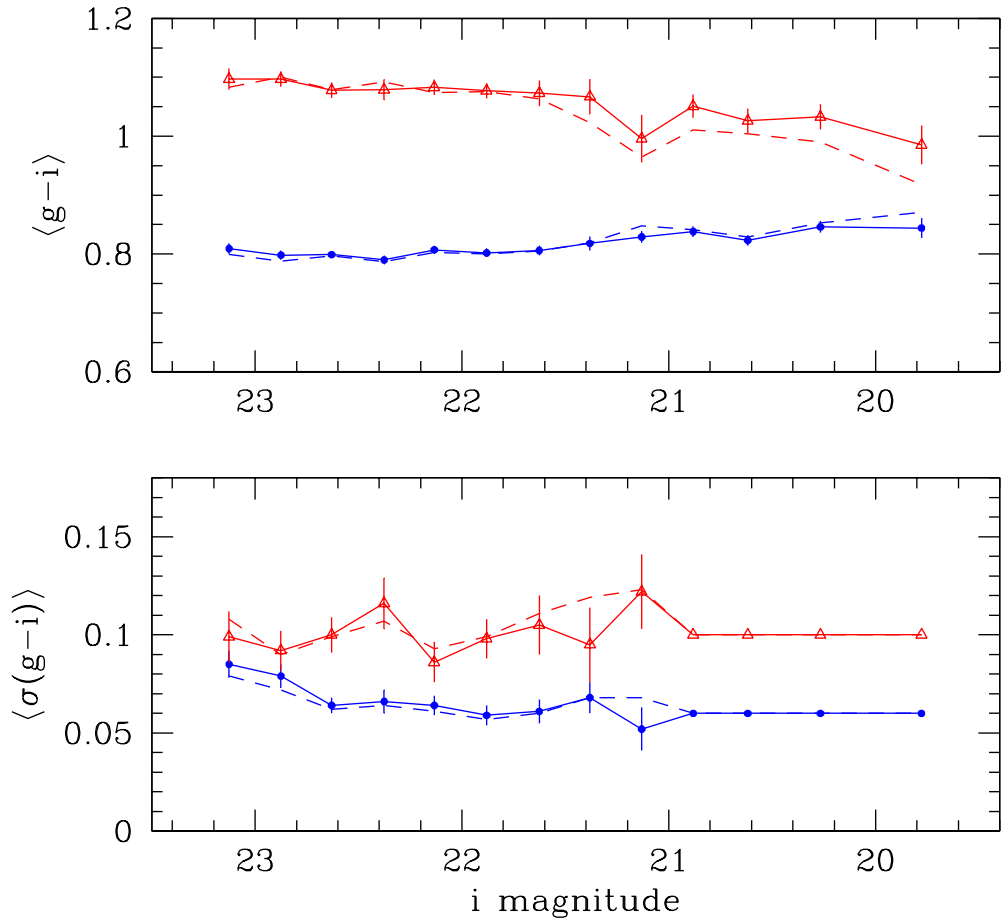


FIG. 9.— *Upper panel:* Binned mean colors in $(g-i)$ for the blue (solid dots) and red (open triangles) sequences, as listed in Table 3. *Lower panel:* Internal standard deviation (color width) of the blue and red sequences as a function of i magnitude. For $i < 21$, the σ -values are constrained at their mean levels (see text). For the blue sequence (lower curve in each panel), the *dashed lines* show how the fitted color and dispersion change if the red sequence is constrained to have $\mu_2 \equiv 1.07$ at all magnitudes, as listed in Table 3. For the red sequence (upper curve in each panel), the dashed lines show the changes if the blue sequence is constrained to have color $\mu_1 \equiv 0.80$ at all magnitudes.

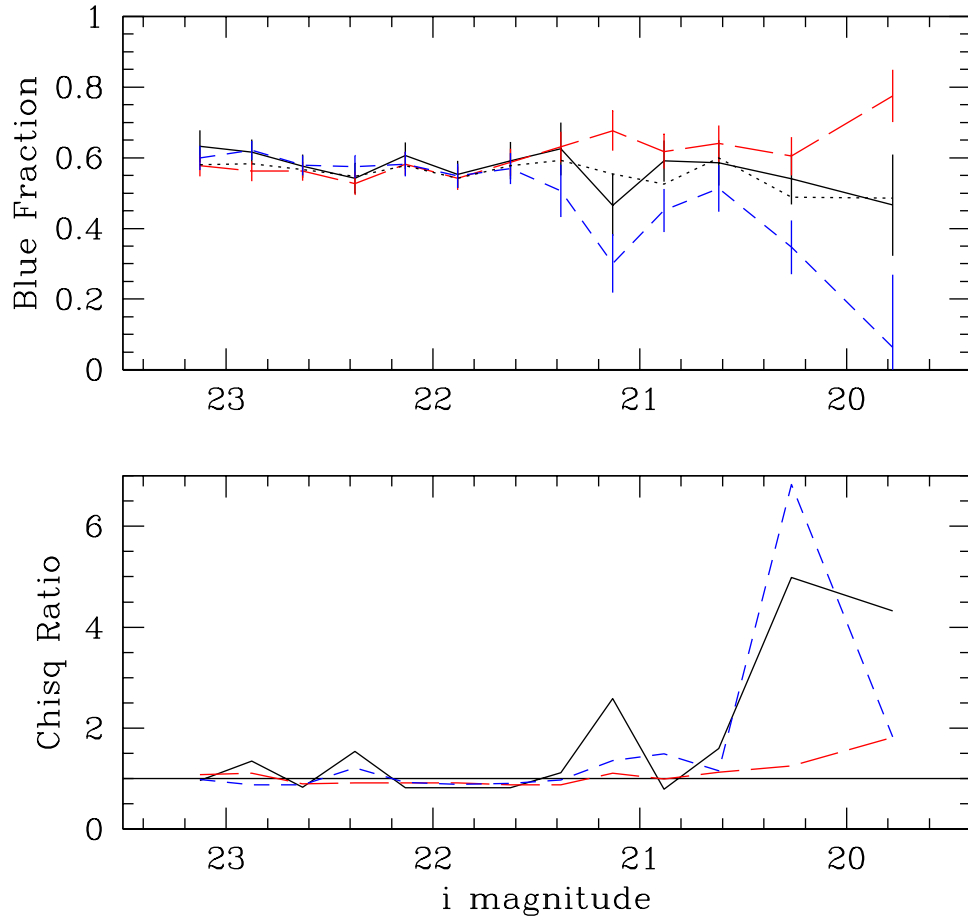


FIG. 10.— *Upper panel:* The fraction p_1 of the total GC population in the blue sequence, plotted as a function of i magnitude and obtained from the bimodal RMIX fits. The solid line shows the results from Table 2, where both blue and red means μ_1, μ_2 are unconstrained. The red long-dashed line shows the results where the red sequence is constrained to lie at $\mu_2 \equiv 1.070$; the blue short-dashed line shows the results where the blue sequence is constrained at $\mu_1 \equiv 0.80$; and the dotted line shows the results where both sequences are constrained. *Lower panel:* The quality-of-fit ratio $\chi^2_{\nu}(\text{constrained})/\chi^2_{\nu}(\text{unconstrained})$ for three different versions of the bimodal-sequence fits. The solid line shows the ratio for the case where both sequences are constrained at $\mu_1 = 0.80, \mu_2 = 1.07$; the red long-dashed line shows the case for $\mu_2 = 1.07$; and the blue short-dashed line shows the case for $\mu_1 = 0.80$. A ratio larger than 1.00 means that the solution provides a worse fit than the unconstrained case.

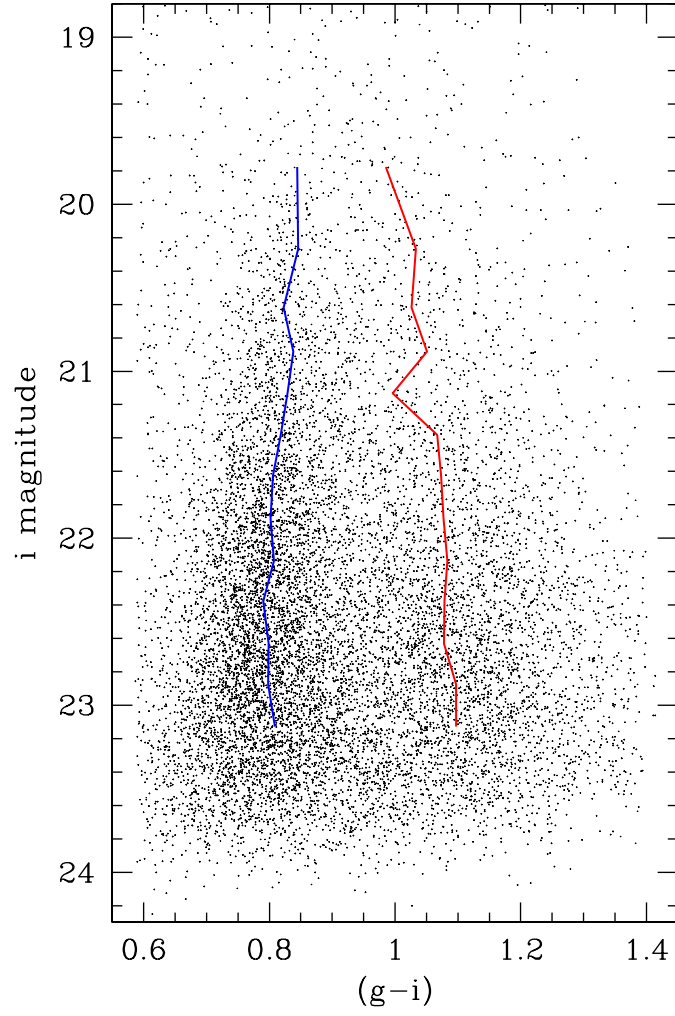


FIG. 11.— Color-magnitude diagram in $(i, g - i)$ for the data used in the bimodal sequence fits (see text). The *solid lines* connect the mean points from Table 3 from the unconstrained bimodal fits.